

# Conformal Volumetric Grayscale Metamaterials

Qinglan Huang, Lucia T. Gan, and Jonathan A. Fan\*

Conformal artificial electromagnetic media that feature tailorable responses as a function of incidence wavelength and angle represent universal components for optical engineering. Conformal grayscale metamaterials are introduced as a new class of volumetric electromagnetic media capable of supporting highly multiplexed responses and arbitrary, curvilinear form factors. Subwavelength-scale voxels based on irregular shapes are designed to accommodate a continuum of dielectric values, enabling the freeform design process to reliably converge to exceptionally high figures of merit (FOMs) for a given multi-objective design problem. Through additive manufacturing of ceramic–polymer composites, microwave metamaterials, designed for the radio-frequency range of 8–12 GHz, are experimentally fabricated and devices with extreme dispersion profiles, an airfoil-shaped beam-steering device, and a broadband, broad-angle conformal carpet cloak, are demonstrated. It is anticipated that conformal volumetric metamaterials will lead to new classes of compact and multifunctional imaging, sensing, and communications systems.

## 1. Introduction

Conformal multifunctional metamaterials that support wave responses as a function of incidence wavelength and angle are enabling technologies for sensing, communication, and imaging where the system's form factor plays as large a role as its electromagnetic response. For aircraft and autonomous cars, systems ideally conform to the shape of the curvilinear vehicle body, which is primarily informed by aerodynamics design. Smart homes require sensors to seamlessly blend in with the environment and have form factors dictated by ergonomics and aesthetics. Optical systems featuring advanced functionality, such as mixed reality devices or ultrawide field of view imaging systems, require non-planar layouts to maximize performance.

There have been several proposed approaches to realize electromagnetic metamaterials that are either conformal or multifunctional. Conformal metamaterials have been fabricated and characterized with thin film metasurfaces that possess a phase response tailored for a given incidence wave condition.<sup>[1]</sup> However, they are fundamentally limited in bandwidth and cannot generalize to support multifunctional operation because they rely on resonators that support local optical responses.<sup>[2]</sup>

Volumetric metamaterials based on transformation optics<sup>[3]</sup> offer wide-angle responses and curvilinear form factors, but they are difficult to extend to arbitrary geometries, require hard-to-achieve material properties, and cannot support arbitrary frequency-multiplexed functions.

Volumetric metamaterials with sub-wavelength-scale material variations optimized through inverse design<sup>[4]</sup> represent a new paradigm that offers the most flexible platform for multifunctionality to date. The term “multifunctional” refers to multiplexed optical responses within a passive (i.e., not tunable) structure that use the same device to produce different optical responses as a function of the frequency, polarization, or wavefront shape of incident light.<sup>[5]</sup> These devices use optimization to leverage volumetric, non-

local wave interactions within the metamaterial bulk, and they have been experimentally demonstrated in a variety of beam steering,<sup>[6]</sup> mode conversion,<sup>[7]</sup> and wavelength splitting tasks.<sup>[8]</sup> However, existing demonstrations remain limited to binary material systems typically with low dielectric contrast,<sup>[9]</sup> which leads to relatively thick devices and limited functional capabilities and efficiencies. Additionally, they are not conformal in part because they are typically designed with Cartesian grid-based features.<sup>[10]</sup> New concepts that incorporate broader degrees of freedom in material topology and composition can lead to qualitatively new metamaterial concepts that support both conformal and multifunctional capabilities.


We introduce a new class of volumetric metamaterial that features conformal form factors, highly multiplexed electromagnetic responses, and exceptionally high efficiencies. Devices are topology optimized using the adjoint variables method,<sup>[11]</sup> which is an iterative gradient-based algorithm that enables unique outgoing wave responses as a function of the wavelength and angle of incident waves. Broadband and broad angle functionality can be realized in wavelength-scale-thick devices, and we experimentally demonstrate a suite of 2D microwave devices fabricated using additive manufacturing, which feature extreme dispersion engineering, conformal carpet cloaking, and frequency-multiplexed beam steering capabilities.

## 2. Results

### 2.1. Implementation of Conformal Grayscale Metamaterials

Our platform achieves unprecedented properties by leveraging metamaterial voxels that possess dielectric constant values

Q. Huang, L. T. Gan, J. A. Fan  
Department of Electrical Engineering  
E.L. Ginzton Laboratory  
Stanford University  
Stanford, CA 94305, USA  
E-mail: jonfan@stanford.edu

 The ORCID identification number(s) for the author(s) of this article can be found under <https://doi.org/10.1002/adma.202204688>.

DOI: 10.1002/adma.202204688

spanning a high contrast grayscale continuum. The grayscale dielectric landscape is advantageous because it offers an expanded design space which supports many exceptionally high performing device designs, many of which are accessible using local gradient-based optimization. It is also a natural design landscape for the adjoint variables method, which requires dielectric constants in each voxel to be initially relaxed to grayscale values, followed by gradient calculations that are used to perturb these values. Our utilization of a wide range of dielectric values ensures that our metamaterial can support strong multiple scattering, which provides the necessary light-matter interactions for high efficiency wavefront engineering in relatively thin devices.<sup>[12]</sup> Our concept is distinct from those currently used for experimental freeform device implementation, where dielectric constant values are explicitly constrained to two discrete values using level set formalisms or regularization terms in the objective function.<sup>[13]</sup>

To practically achieve grayscale dielectric values in our metamaterial, we utilize a hierarchical material architecture approach, outlined in **Figure 1**. First, the freeform device is discretized into triangular or quadrilateral voxels with a critical dimension of approximately  $\lambda/10$ . A freeform discretization based on finite element method meshing<sup>[14]</sup> ensures that the discretized device captures a high-quality reconstruction of the desired shape curvature. Second, the voxels are further discretized into a series of horizontal thin films, each with a

thickness of approximately  $\lambda/100$  and each possessing dielectric constant values of either  $\epsilon_1$  or  $\epsilon_2$ . At this extreme subwavelength length scale, the dielectric response of each voxel for transverse electric (TE) polarized fields (i.e., fields perpendicular to the film stack) can be described with the effective medium theory (EMT):<sup>[15]</sup>  $\epsilon_{\text{eff}}^{-1} = f\epsilon_1^{-1} + (1-f)\epsilon_2^{-1}$ , where  $f$  is the fill fraction of  $\epsilon_1$ .

We experimentally demonstrate our idea in the X band (8–12 GHz), which is a common testbed for electromagnetic metamaterial studies<sup>[3,16]</sup> and is relevant for radar and wireless communications technologies. Devices are fabricated using additive manufacturing methods based on fused filament fabrication (Figure 1b). The manufacturing apparatus can print two types of ceramic-doped acrylonitrile butadiene styrene (ABS) filaments with high and low dielectric constant values, respectively. Detailed characterization (Section 4) indicates that the dielectric constant values of bulk materials printed from the two filament types are  $\epsilon_1 = 2.67$  and  $\epsilon_2 = 8.40$ , respectively. The spatial resolution of the extruded filaments is 250  $\mu\text{m}$ , which ensures that the multilayer voxels within the metamaterial have responses well into the effective medium limit at our frequencies of interest. To evaluate device performance, we map the electromagnetic fields using a near-field scanning apparatus<sup>[17]</sup> comprising a parallel plate waveguide that supports the fundamental TE mode in the X band (Figure 1c). Electromagnetic wave excitations are introduced into the waveguide using either a coaxial antenna or a coaxial-to-waveguide adapter (Section 4).

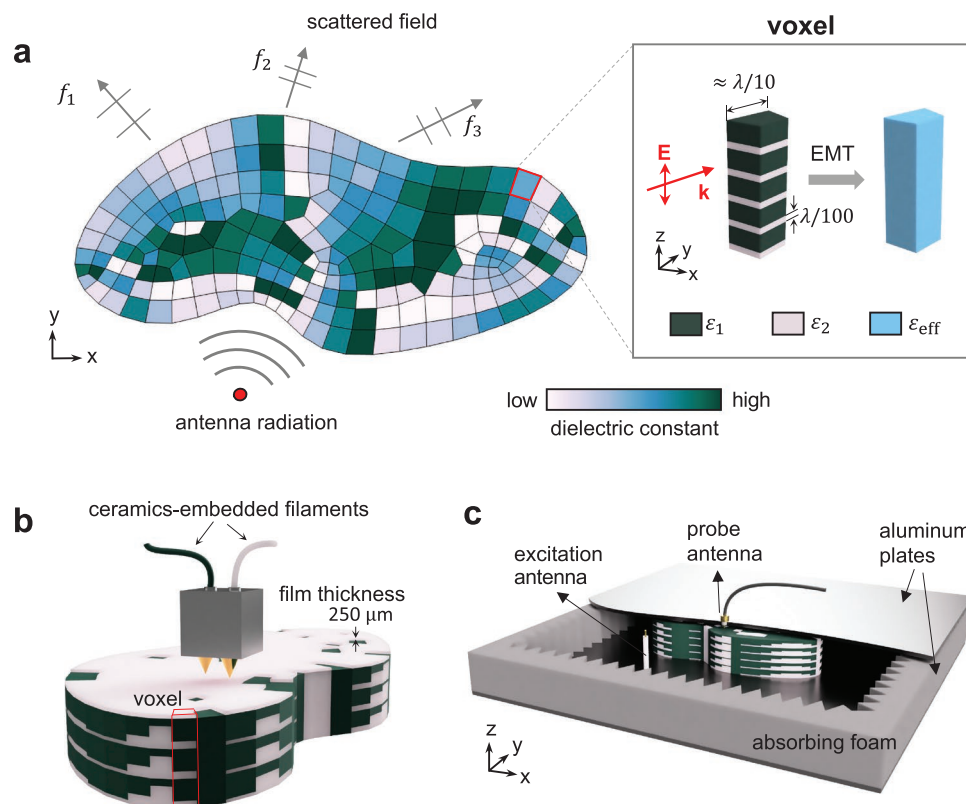


**Figure 1.** Framework of conformal volumetric grayscale metamaterials. a) Conceptual illustration of a freeform grayscale metamaterial with frequency-multiplexed functionalities. The volumetric metamaterial is composed of irregularly shaped subwavelength-scale voxels with effective grayscale dielectric constant values that are specified using gradient-based optimization. Inset: each voxel comprises an ultra-subwavelength-scale dielectric composite that yields grayscale dielectric values in the EMT limit. b) Schematic of the grayscale metamaterial fabrication process via additive manufacturing. c) Schematic of the near-field scanning setup used for metamaterial characterization.

The complex electric field distribution is measured by mechanically scanning a probe antenna attached to the top aluminum plate.

## 2.2. The Grayscale Dielectric Landscape

To quantify the advantages of the grayscale dielectric landscape for electromagnetic device design, we systematically investigate volumetric metagratings as a model system. The optimization objective is to maximize the diffraction efficiency, defined as the power diffracted into the  $-1$  order normalized to the input power, for a normally incident TE wave at  $\lambda = 30$  mm (Figure 2a). Efficiency histograms of two types of devices designed using gradient-based optimization, one comprising a continuous grayscale dielectric distribution and the other a binary dielectric distribution, is summarized in Figure 2b. For each device type, 100 devices are designed with random initial dielectric distributions. The efficiency histograms for binary devices span a wide range of values, indicating that the optimization landscape comprises many local optima with widely varying efficiencies. The best binary device

has an efficiency of 87.0% and the associated near-field distribution shows aberrated outgoing wavefronts (Figure 2b inset). On the other hand, the distribution of grayscale device efficiencies is strongly peaked near 99.9%, indicating that local gradient-based design algorithms are effective and computationally efficient for these devices. Interestingly, these high performing devices all have widely varying layouts (Figure S2, Supporting Information), indicating that while the optimization landscape is non-convex, there exist many local optima featuring exceptional performance. A field plot of the outgoing wave for the best grayscale device shows an ideal planewave profile with no discernable aberration (Figure 2b inset).

High dielectric contrast plays a significant role in dramatically reducing the thickness of high performing metamaterials, which is particularly important in microwave devices where wavelengths are centimeter-scale. To quantify this, we optimize fully grayscale metagratings with a range of thicknesses and dielectric contrast values, which we define as  $\Delta\epsilon = \epsilon_{\max} - \epsilon_{\min}$  with  $\epsilon_{\min} = 2.67$ . The voxel dimensions are fixed to  $\lambda/20$ . The threshold device thicknesses required to realize device designs with 99% device efficiencies as a function of  $\Delta\epsilon$  are plotted in Figure 2c. When  $\Delta\epsilon$  is low, the device thicknesses are required

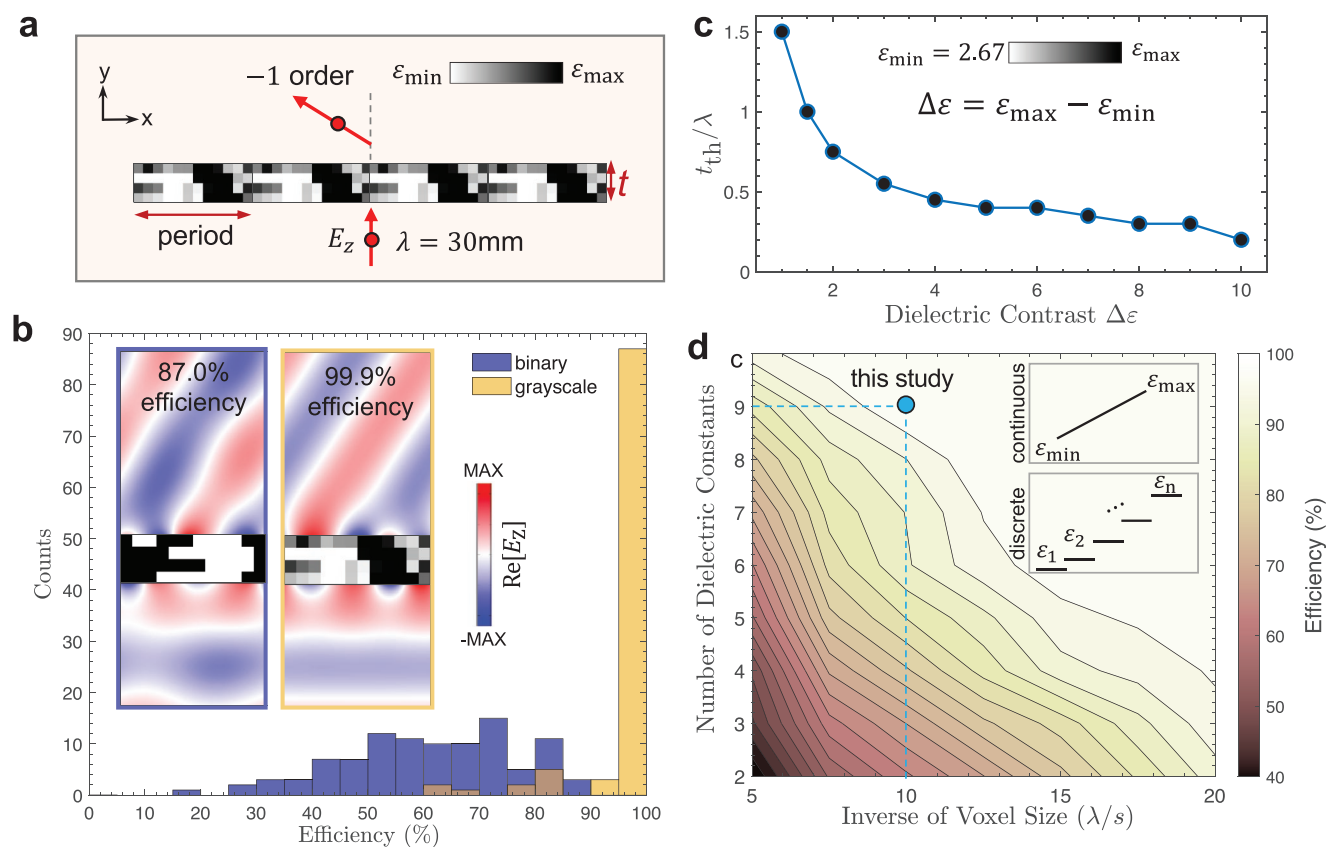


**Figure 2.** Analysis of the grayscale dielectric design space. a) Schematic of a periodic volumetric metagrating, serving as our model system, which selectively diffracts a normally incident beam to the  $-1$  diffraction order. b) Histograms of diffraction efficiencies for topology-optimized metagratings comprising binary and grayscale dielectric distributions. For both device types, the device thickness is  $0.4\lambda$  and optimization is performed on 100 randomly initialized dielectric distributions. Insets: single unit cell device layouts, electric field responses, and diffraction efficiencies of the best binary (blue box) and grayscale (yellow box) devices from the histograms. c) Threshold device thickness,  $t_{\text{th}}$ , required for an optimized grayscale metagrating to achieve 99% efficiency, as a function of dielectric contrast. d) Contour plot of device efficiency as a function of voxel size and number of discrete dielectric values used in the designs. The label “c” in the y-axis stands for continuous grayscale distribution. The device parameters used for further metamaterial design in this study are denoted. Inset: illustration of continuous and discrete dielectric constant values.

to be on the order of or greater than the wavelength. While these devices utilize non-local interactions to tailor the phase response, light–matter interactions are limited to scattering and waveguiding phenomena in the forward direction (Figure S3, Supporting Information). As  $\Delta\epsilon$  increases, the minimum device thickness drops over  $7\times$  to values much less than the wavelength. These thickness reductions are due not only to enhanced field compression and confinement in high dielectric constant regions, but also to strong multiple scattering effects that enable higher quality factor modes and particularly strong non-local waveguiding effects (Figure S3, Supporting Information). In this regime, the metamaterial operates with efficiencies and multifunctional capabilities far beyond the limits of metasurfaces that rely on local field interactions.<sup>[2a]</sup>

A parametric analysis of metagratings as a function of voxel size and dielectric discretization, shown in Figure 2d, indicates that devices comprising multiple discrete dielectric values have efficiencies that effectively converge to those of grayscale designs. This functional equivalence between multimaterial and grayscale metamaterials is important because in practice, the voxel films fabricated from the additive manufacturing process have finite thickness that prevents continuous tuning of  $\epsilon_{\text{eff}}$ . In the limit where the smallest simulated voxel size is  $\lambda/20$ , device efficiency converges to that of continuously grayscale devices, even when number of discrete dielectric values is small. Here, ensembles of voxels in the  $x$ – $y$  device plane have electromagnetic properties that can be effectively homogenized in the grayscale limit. As voxel size increases, metagratings possessing discrete dielectric values can only operate as efficiently as those with grayscale values with sufficiently large number of materials. In this study, we will be considering devices comprising voxels with  $\lambda/10$  and nine possible dielectric values between  $\epsilon_1 = 2.67$  and  $\epsilon_2 = 8.40$ , and they exhibit the same efficiencies as their grayscale counterparts. As our devices are optimized primarily in the continuous grayscale landscape and dielectric discretization negligibly changes the device layout or performance, we consider them to be effectively operating in the grayscale limit.

### 2.3. Applications and Demonstrations

In our first set of device demonstrations, we show that volumetric metamaterials can be configured to support beam deflection behavior with nearly arbitrary dispersion responses. Materials featuring customizable dispersion are critical for many electromagnetic systems, where they are used to compensate for chromatic aberrations, can enhance spectral resolution for spectroscopic applications, and can directly provide achromatic wavefront shaping capabilities.<sup>[18]</sup> Theoretical results for three types of optimized grayscale metamaterials are shown in Figure 3a–c. These devices are designed to exhibit unusual dispersion profiles spanning the X band and they include a linear positive profile, quadratic positive profile, and a hybrid profile that is linear negative followed by linear positive. Such profiles exceed the capabilities of traditional metasurface dispersion engineering approaches, which are limited by the local optical responses of subwavelength-scale waveguide and resonator elements.<sup>[19]</sup> The good agreement between the target scattering

angles and device scattering profiles, and their strong directional scattering characteristics, indicate the potential of grayscale volumetric metamaterials to perform extreme dispersion tasks.

To demonstrate that these concepts can be readily implemented in a physical device, we experimentally fabricate and characterize an achromatic device that deflects normal incident fields to  $\theta = 30^\circ$  for all X band frequencies. The device has dimensions of  $240\text{ mm} \times 42\text{ mm} \times 10\text{ mm}$  and the voxels are squares with edge dimensions of  $3\text{ mm}$ . The grayscale dielectric distribution of the device is shown in Figure 3d, and the printed device is shown in Figure 3e. The experimentally measured scattering profiles (Figure 3f), which are obtained using a near-to-far field transformation<sup>[20]</sup> at the device exit plane, clearly demonstrate efficient achromatic scattering across the full X band. The measured electric field maps at two representative frequencies,  $f_1 = 8.85\text{ GHz}$  (Figure 3g) and  $f_2 = 10.58\text{ GHz}$  (Figure 3j), display complex mode dynamics within the volumetric metasurface that enable efficient conversion of the normally incident wavefronts into deflected wavefronts.

These experimental results are consistent with simulated field maps (Figure 3h,k), which assume an incident plane wave and show clear directional scattering of the output fields to the desired deflection angle. Small discrepancies between the simulated and measured fields within the device region are due to deviations of the experimental incident wave from an ideal plane wave (Figure S5, Supporting Information). This agreement indicates that the fabricated device faithfully reproduces the designed grayscale dielectric profile and that such agreement should extend to other device types, including those supporting other types of dispersion profiles (Figure 3a–c) and even more complex functionality. The strong non-local light–matter interactions that enable achromatic scattering are visualized in theoretical plots of power flux in Figure 3j,l, which show waves propagating in meandering pathways throughout the metamaterial volume. These light–matter interactions are qualitatively different from power flow in conventional local metamaterials, and they reveal how large amounts of phase can accumulate to enable broadband functionality within our relatively thin metamaterial.

Frequency-multiplexed wavefront engineering can be readily extended to devices with arbitrary curvilinear layouts, thereby enabling new classes of systems that simultaneously support electromagnetic and non-electromagnetic properties. As a proof-of-concept demonstration, we design and implement a volumetric beam forming metamaterial that is shaped as a miniaturized airfoil. The device shape, optimized for aerodynamics, is directly adopted from ref. [21] and occupies a footprint of  $240\text{ mm} \times 70\text{ mm}$ . Beam forming is achieved using an embedded radiation antenna as the source and designing the metamaterial to collimate and steer the emitted radiation to different directions as a linear function of the signal frequency. A perfect electric conductor (PEC) boundary at the bottom surface of the device prevents radiation leakage in this direction. The optimized grayscale dielectric distribution of the metamaterial and an image of the manufactured device are shown in Figure 4a,b, respectively.

Experimental field scans of the device as a function of antenna frequency show excellent agreement between theory

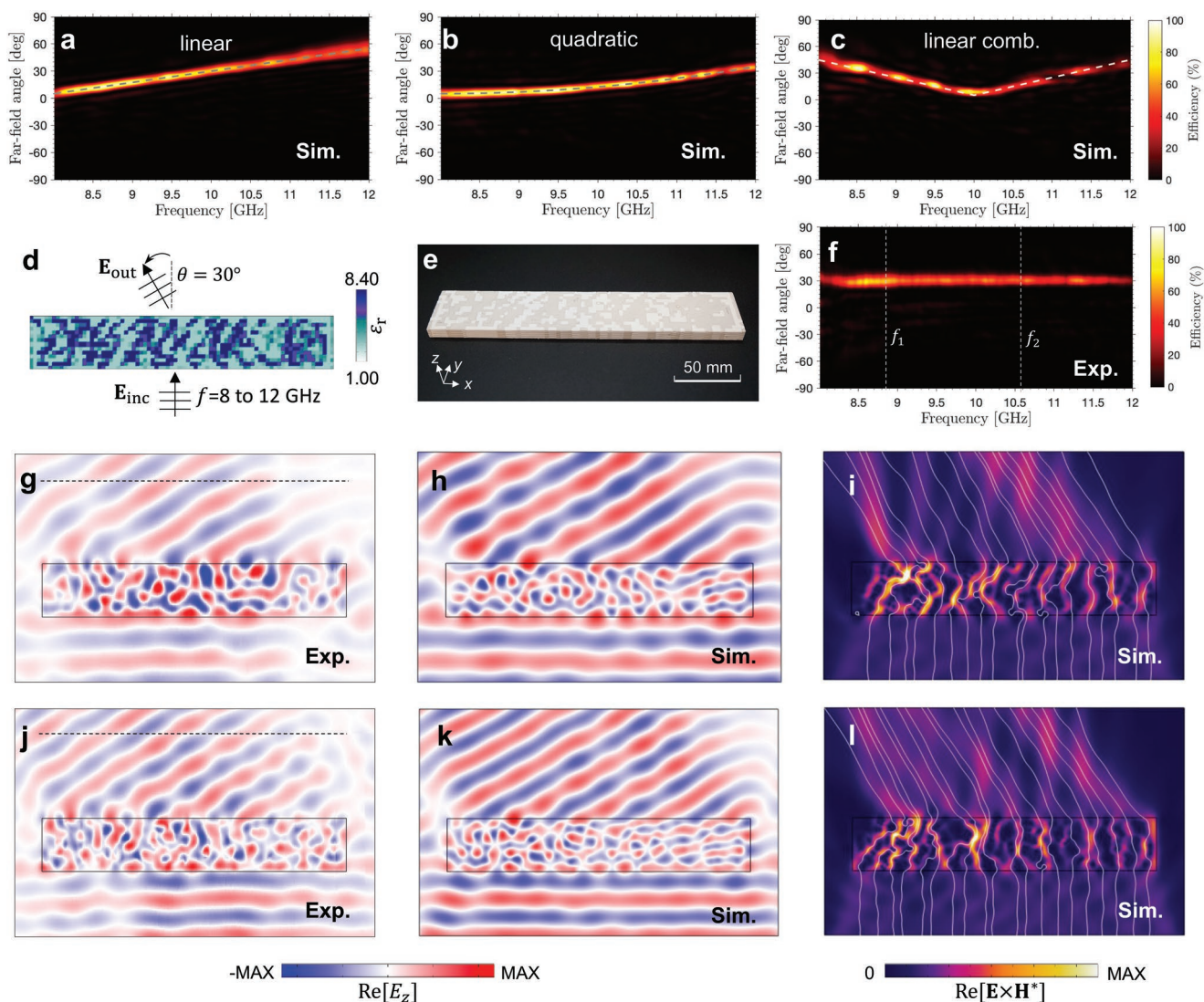


**Figure 3.** Dispersion engineering in metamaterial scatterers. a–c) Simulated far-field properties of three inverse designed grayscale metamaterials, operating across the X band, with positive linear (a), positive quadratic (b), and a combination of positive and negative (c) linear dispersion profiles. d) Dielectric distribution of a grayscale metamaterial that achromatically scatters normal incident fields toward  $\theta = 30^\circ$ . e) Image of the additively manufactured achromatic scatterer. The device dimension is 240 mm  $\times$  42 mm  $\times$  10 mm. f) Experimentally measured far-field scattering properties of the achromatic metamaterial, which shows a constant far-field scattering angle as a function of frequency. The dashed lines denote  $f_1 = 8.85$  GHz and  $f_2 = 10.58$  GHz. g–i) Experimentally measured near-field distribution (g) and simulated near-field distribution (h) and power flow (i) at  $f_1$ . The solid lines and colormap in (i) show the direction and magnitude of the Poynting vector, respectively. j–l) Same as (g–i) but at  $f_2$ . The dashed lines in (g) and (j) denote the exit plane position used for the near-to-far field transformation calculations in the far-field scattering plots.

and experiment. A comparison of the far-field power distribution as a function of frequency, obtained using a near-to-far field transformation of the scanned fields, shows highly efficient beam deflection to the desired angle in a manner that matches theoretical far-field predictions (Figures 4c,d). The ability of our device to perform beam steering from  $-20^\circ$  to  $+20^\circ$  with only a 10% change in frequency showcases the potential of our platform to support strong super-prism-like effects<sup>[22]</sup> in a manner that is decoupled from the device's form factor. The divergence of the collimated beams is  $8.0^\circ$  at the central frequency, which corresponds to an aperture of 240 mm that matches the device width. As such, the extreme non-local light–matter interactions manifested in the metamaterial can enable aperture-limited

beam forming despite the point nature of the source and the unusual shape of the device. Representative near-field distributions at three different frequencies (Figures 4e–g) show clear collimation directed toward the intended target direction. Simulated near-field distributions as the frequency is continuously swept from 10 to 12 GHz are shown in Movie S1, Supporting Information.

Finally, we experimentally demonstrate a compact invisibility carpet cloak that is conformal to an arbitrarily shaped object. As shown in Figure 5a,b, the optimized device has a two-wavelength-thick footprint, and it conformally covers an asymmetrically shaped object with a geometry represented by the Cubic Bézier spline. The grayscale carpet cloak renders

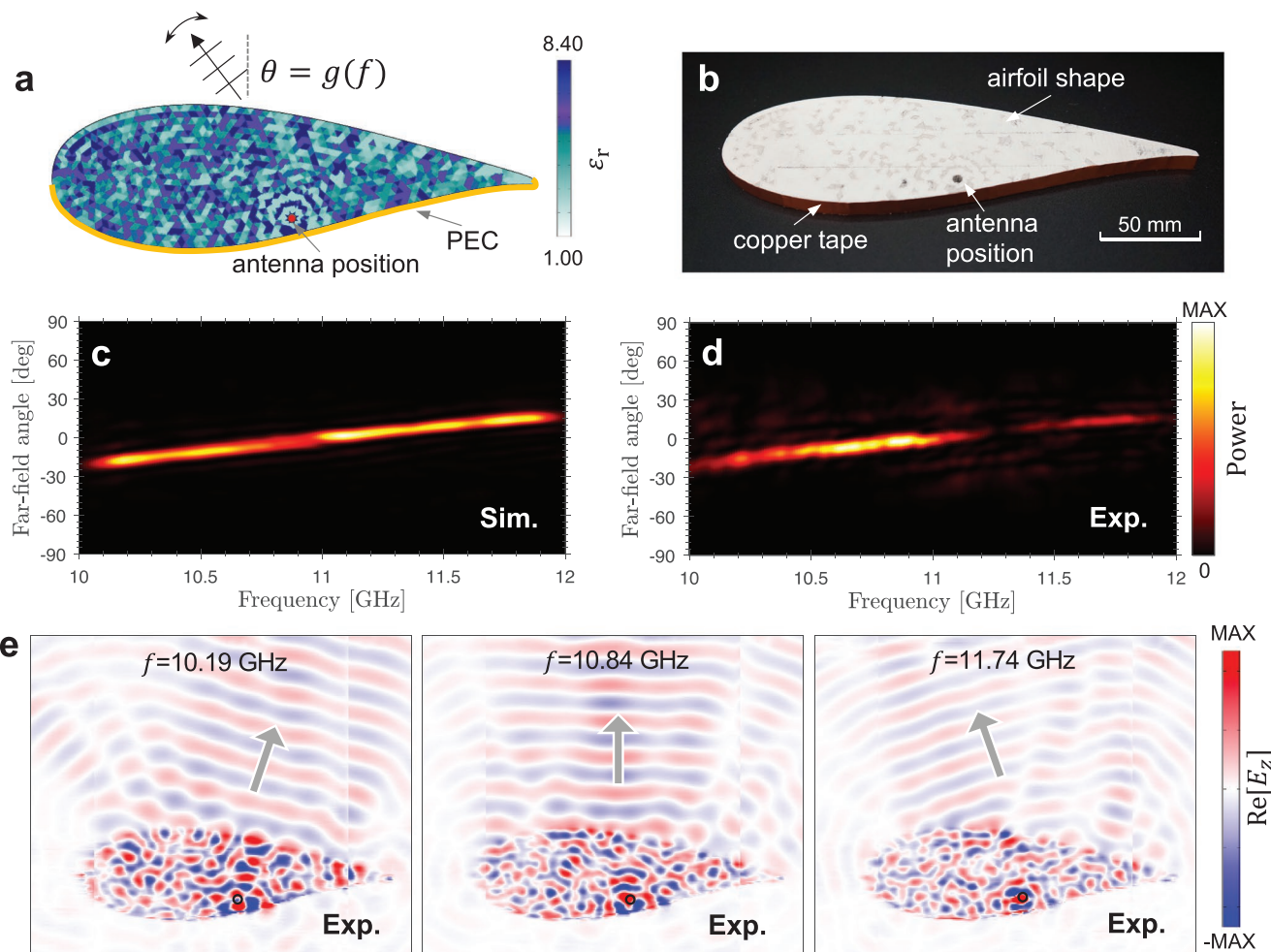


**Figure 4.** Beam forming and steering with an embedded line source in an airfoil-shaped metamaterial. a) Dielectric distribution of an airfoil-shaped beam former that collimates and steers radiation from a coaxial antenna to different far-field directions as a function of frequency. b) Image of the additively manufactured airfoil-shaped beam former. c,d) Simulated (c) and experimentally measured (d) far-field properties of the airfoil device. The far-field profiles were calculated using near-to-far-field transformations from the scattering near-field profiles. e) Measured electric near-field profiles at three different frequencies. The antenna position is marked by the black circle.

the object invisible by restoring the phase of the reflected wave as to mimic the ground plane response, and it is responsive to incident waves featuring frequencies ranging from 10 to 11 GHz and incident angle ranging from  $-30^\circ$  to  $+30^\circ$ . Our cloaking approach aims to address limitations posed by existing methods based on coordinate transformations,<sup>[23]</sup> which require complex-valued permittivity and permeability parameters for implementation and are difficult to generalize to arbitrary shapes.<sup>[24]</sup> It also aims to improve on existing carpet cloak concepts, which can introduce non-ideal phase shifts in the scattered light wave response.

Theoretical field plots indicate that the optimized device exhibits excellent invisibility to planewaves as a function of frequency and angle of incidence (Figure S6 and Movie S2, Supporting Information). Experimental scans of the cloak with a collimated incident beam, for different frequencies and angles of incidence, are summarized in Figure 5c–f and show that the scattered field profiles match those of an incident wave reflecting from a flat ground plane. Furthermore, the simulated (Figure 5e) and measured (Figure 5f) field profiles are in

excellent agreement. We note that as our device operates for a broad range of frequencies and angles, its invisibility functionality readily extends to incident sources with a diversity of temporal and spatial profiles, due to the linearity of Maxwell's equations. Our device therefore works well for a variety of incident Gaussian waveforms and can conceal the object from one or multiple point sources (Figures S7 and S8, Supporting Information).

Our invisibility cloak presents clear advantages to leading cloaking concepts based on transformation optics.<sup>[3,23]</sup> First, cloaks based on transformation optics support a narrow range of observation angles about the axis of the coordinate transformation, whereas our inverse designed cloak supports a  $60^\circ$  field of view. Second, transformation optics-based metamaterials are typically constructed using split ring resonators, which are dispersive and therefore yield a narrow operational bandwidth and absorption losses. In contrast, our inverse designed dielectric cloak is lossless and presents no fundamental limit in bandwidth. Third, transformation optics-based cloaks are often impedance mismatched to the surrounding environment,

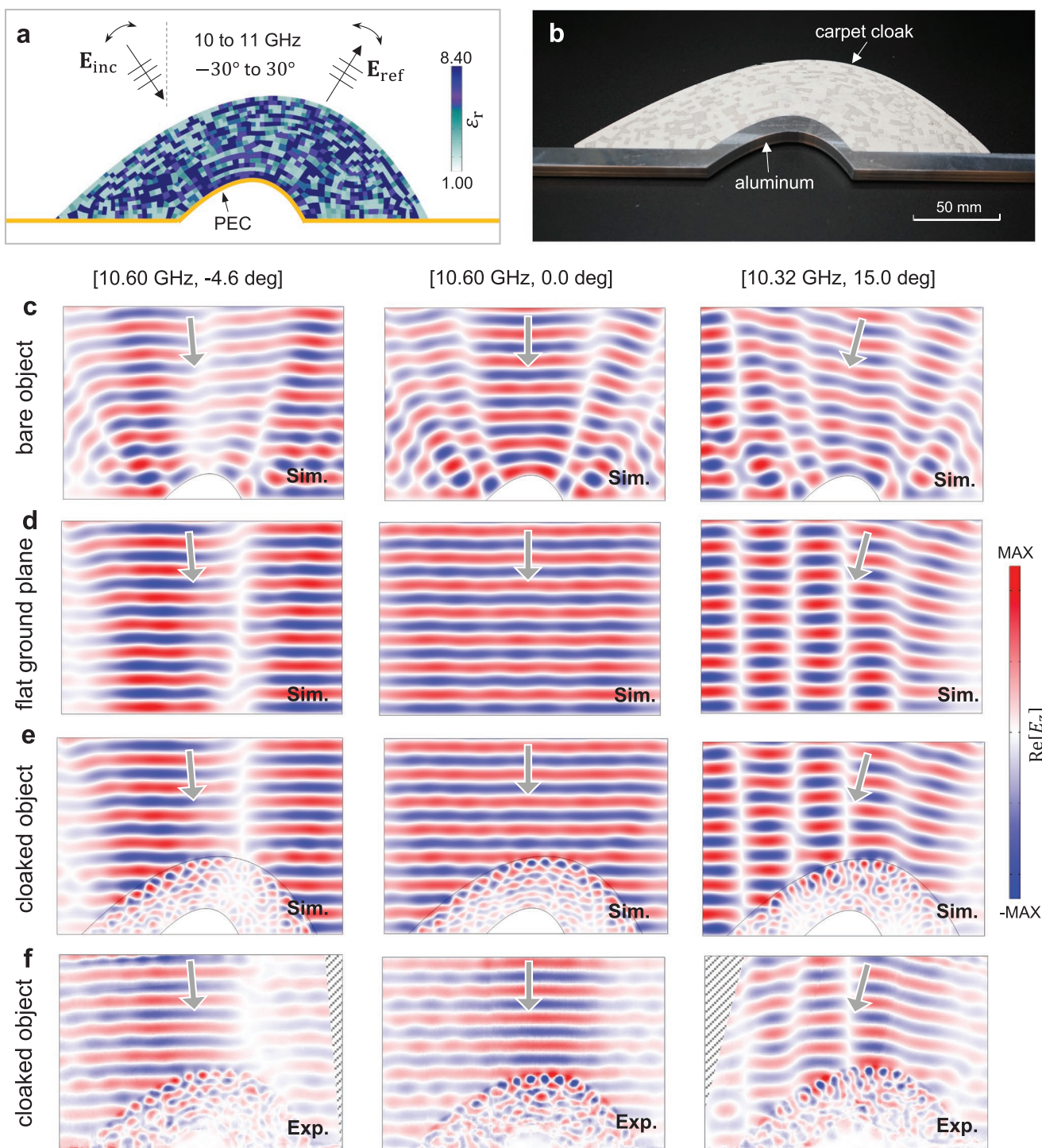


**Figure 5.** Conformal carpet cloak. a) Design of a ground plane cloak that is conformal to an asymmetric, perfectly electrically conducting scatterer. The cloak is specified to operate for incident angles spanning  $-30^\circ$  to  $30^\circ$  and frequencies spanning 10 to 11 GHz. b) Image of the additively manufactured cloak and asymmetric curvilinear metallic scatterer with ground plane. c–f) Simulated near-field distributions of the bare scatterer with ground plane (c), flat ground plane with no scatterer (d), and scatterer with the conformal cloak (e). The experimental near-field distributions of the scatterer with the conformal cloak (f) agree well with the simulated results in (e). The figures include data for three different frequencies and/or incident angles, and the incident angles are denoted in the field plots by gray arrows. The hatched regions in (f) are regions that were not scanned due to limitations in scanning area in our measurement apparatus.

whereas interfacial reflection is automatically minimized in our device through the optimization process. Finally, a con-

formal cloak based on transformation optics requires materials featuring hard-to-obtain permittivity and permeability tensor

values, while our grayscale metamaterial utilizes standard dielectric materials.

### 3. Conclusion

We introduce grayscale conformal metamaterials that exhibit high efficiency, multiplexed optical responses as a function of wavelength and incidence angle. Our use of high contrast grayscale dielectrics is essential to yielding design spaces that support exceptionally high performing devices, which can be identified using standard gradient-based optimization methods. Our demonstration of carpet cloaks and an airfoil-shaped beam former with wavelength-thick metamaterials indicates the potential for our platform to support advanced optical functionality with compact form factors. Looking ahead, we anticipate that grayscale metamaterials will serve as ideal components for optical analog computing,<sup>[9b,25]</sup> communications,<sup>[26]</sup> ranging,<sup>[27]</sup> imaging, and sensing applications. They are particularly well suited for systems in which the optical hardware and software are codesigned to perform a specific task, as the gradient-based design method for the metamaterials can be readily integrated into end-to-end design algorithms based on backpropagation.<sup>[28]</sup> While our study focuses on 2D devices, the concepts can readily extend to 3D electromagnetic systems. It is possible to design polarization insensitive, or even polarization multiplexed devices based on the grayscale metamaterial concept. In this regard, the metamaterial voxels need to be designed to produce isotropic or anisotropic dielectric response. Our concepts can readily extend to other frequency ranges due to the scalability of Maxwell's equations, and we anticipate that the emergence of new multimaterial additive manufacturing techniques<sup>[29]</sup> can lead to the experimental realization of large volume devices operating at frequencies beyond the microwave. While an all-metamaterial approach will be suitable for many applications, we foresee that hybrid optical systems that synergistically combine grayscale metamaterials with refractive and scalar diffractive optics will further enhance bandwidth, aberration correction, and functional multiplexing capabilities.

### 4. Experimental Section

**Complex Permittivity Characterization:** Two ceramic-embedded filaments (ABS 300 and ABS 1200 from Avient Corporation) were implemented in our experiments. The complex dielectric constants of the extruded materials were characterized using the filled waveguide method.<sup>[30]</sup> The measurement setup consisted of a network analyzer (Rohde & Schwarz ZNB20), coaxial cables extending from the VNA ports to WR-90 waveguide adapters, and a 10 mm-long waveguide section filled with the printed block to be characterized. A thru-reflect-line (TRL) calibration was performed to obtain optimal results using a waveguide short as a reflect standard and a 10 mm-long waveguide shim as the line standard. Once the calibration was performed, all four *S* parameters of the filled waveguide were measured and then used the NRW algorithm<sup>[31]</sup> to extract the complex dielectric constant from the *S* parameters. The extracted complex dielectric constants of the two filaments are plotted in Figure S1a, Supporting Information, and show high dielectric constant contrast and extremely low loss across the X band.

The grayscale voxel was formed by vertically stacking thin film layers of the filament material, each with a thickness of 250 μm. Eight layers were used to produce a supercell with a thickness  $\Lambda = 2$  mm such that

nine different fill fraction combinations, ranging from all ABS 300 to all ABS 1200, were considered. Five supercells were then vertically stacked to produce a 10 mm-tall voxel. Within each voxel,  $\Lambda \ll \lambda$  and the layered media was squarely in the effective medium limit and away from the photonic crystal regime ( $\Lambda \sim \lambda$ ). Maxwell–Garnett EMT predicts that the multilayer effective dielectric constants with TE polarization (electric field polarized perpendicular to the layers) follow  $\epsilon_{\text{eff}}^{-1} = f\epsilon_1^{-1} + (1-f)\epsilon_2^{-1}$ , where *f* is the fill fraction of  $\epsilon_1$ . The parallel plate waveguide enforced TE polarization in these experiments. The effective dielectric constants achievable in these voxels are shown as the blue curve in Figure S1b, Supporting Information.

In this experiment, a 120 μm air gap between the device and top aluminum plate provided space to enable smooth mechanical translation of the plates during scanning. As such, the guided electromagnetic wave within the parallel waveguide interacted with the 3D printed device plus this air gap. While the air gap was sufficiently thin as to not modify the mode distribution within the device, it did reduce the effective dielectric constant experienced by the guided wave. To account for this effect, an additional step of EMT that accounts for the air gap was performed, as shown with the orange curve in Figure S1b, Supporting Information. Our final minimum and maximum dielectric constants in this EMT limit are 2.67 and 8.40, respectively.

**Topology Optimization:** The dielectric distribution of a functional device was generated through gradient-based inverse design. First, the design domain defined by an arbitrary conformal form factor was discretized into spatial grids, or voxels, whose size were on the order of one tens of a vacuum wavelength. To ensure accurate representation of the curvilinear profile without stitching error, the finite element method meshing algorithm was adopted to generate voxels with triangular or trapezoidal shapes. Each voxel was then assigned a dielectric constant value through topology optimization described as follows.

The design started with a random initial dielectric constant distribution  $\epsilon(\mathbf{x}, \mathbf{y})$ , which was then perturbatively improved over a series of iterations to optimize the merit function. In this work, the figure of merit (FOM) was defined as the overlap between the output electric field at the exit plane of the device, with the “target” field.<sup>[32]</sup> Specifically, the plane-wave decomposition at the exit plane is given by

$$\mathbf{E}(\mathbf{x}) = \frac{1}{A} \sum_i c_i \hat{\mathbf{y}} e^{i\mathbf{k}_i \cdot \mathbf{x}} = \sum_i c_i \mathbf{E}_i(\mathbf{x}) \quad (1)$$

where  $\mathbf{k}_i$  is the wavevector for each plane wave, *i* is a discretized order of composing angle, and  $\hat{\mathbf{y}}$  is the unit vector of TE polarization. The target electric field is given by

$$\mathbf{E}^{\text{tar}}(\mathbf{x}) = \frac{1}{A} \sum_i c_i^{\text{tar}} \hat{\mathbf{y}} e^{i\mathbf{k}_i \cdot \mathbf{x}} = \sum_i c_i^{\text{tar}} \mathbf{E}_i(\mathbf{x}) \quad (2)$$

The FOM is then

$$f = \left| \int_{-\frac{A}{2}}^{\frac{A}{2}} \mathbf{E}^* \cdot \mathbf{E}^{\text{tar}} \, dx \right|^2 = \sum_i |c_i^* c_i^{\text{tar}}|^2 \quad (3)$$

Equation (3) is a function of frequency and incident angle, and independent of the relative phase between the output and desired electric fields. To optimize the multifunctional performance, Equation (3) is maximized over a range of frequency and incident angle average. To achieve a uniform performance over the broadband and wide angle, the set of frequency and incident angle were randomly jittered in each iteration. This approach avoided “hot spot” at isolated frequencies and incident angles but poor performance in between.

The sensitivity,  $\frac{df}{d\epsilon}(\mathbf{x})$ , is computed from the electromagnetic fields in two full wave simulations using COMSOL Multiphysics:<sup>[33]</sup>

$$\frac{df}{d\epsilon}(\mathbf{r}) = \text{Re} \{ \mathbf{E}_{\text{fwd}}(\mathbf{r}) \cdot \mathbf{E}_{\text{adj}}(\mathbf{r}) \} \quad (4)$$



where the forward field  $E_{\text{fwd}}(\mathbf{r})$  is the electric fields within the device when illuminated with incident waves, and the adjoint field  $E_{\text{adj}}(\mathbf{r})$  is the electric fields within the device when illuminated with the time-reversed target electric fields. The sensitivity for multiple frequencies and incident angle were simultaneously calculated. Then the mean sensitivity was used to update the dielectric profile via gradient decent:

$$\varepsilon_{j+1}(\mathbf{x}, \mathbf{y}) = \varepsilon_j(\mathbf{x}, \mathbf{y}) + \alpha \sum_{\lambda, \theta} \frac{df}{d\varepsilon}(\mathbf{r}) \quad (5)$$

During the optimization, a 9-level dielectric constant discretization was enforced to comply with these fabrication constraints. A sigmoid-like projection function with gradually increasing strength was used to push the dielectric constants to nine distinct values achievable in this 3D printing process. Now the 2D dielectric distribution of the device was obtained.

**Device Fabrication:** Next, the 2D dielectric distribution was translated into a 3D material stack for each voxel via the EMT as described in the main text. A computer aided design (CAD) drawing of the design was constructed in AUTODESK Fusion 360 via python scripting. The devices were printed on a Raise 3D printer. Low and high dielectric constant filaments were fed into the two nozzles of the printer, respectively. The 3D STL files were uploaded to the 3D printer control software and sliced. Slicing converts the STL file to G code, which dictates the path followed by the 3D printer nozzle. The printing parameters such as temperature, layer height, linewidth, and wall thickness were set to optimize the print quality.

**Near-Field Mapping:** Near-field characterization of the metamaterial was carried out in a 2D X-band parallel-plate waveguide which consists of two aluminum plates separated by a gap of  $h = 10.12$  mm. The VNA feeds the signal to the source and detects the  $S$  parameters data ( $S_{21}$ ), whose spatial mapping is the complex electric field distribution. Two excitation methods were implemented for either a line source excitation or Gaussian beam excitation. For a line source excitation, which is used for the airfoil experiment, a coaxial probe on the lower plate excited a radial wave within the chamber. For a Gaussian beam excitation, which is used for the scatterer and cloaking experiments, radiation was introduced through a coaxial-to-waveguide adapter equipped on the edge of the lower plate and then collimated by a dielectric parabolic lens (Figure S5, Supporting Information). The waveguide only supported the fundamental TEM mode. The measured field maps were stitched from three fixed probe antennas equipped on the top aluminum plates. The lower aluminum plate was attached to optical motion stages (Thorlabs) that spatially translate the sample relative to the probe antennas. To avoid reflection from the boundary of the waveguides, a 10 mm-thick absorption foam was cut in a sawtooth pattern and arranged along the edges of the lower plate. Further details of the apparatus can be found elsewhere.<sup>[17]</sup>

## Supporting Information

Supporting Information is available from the Wiley Online Library or from the author.

## Acknowledgements

This work was supported by the National Aeronautics and Space Administration under award no. 80NSSC21K0220, the Air Force Office of Scientific Research under award no. FA9550-18-1-0070, and the Office of Naval Research under Award Number N00014-20-1-2105.

## Conflict of Interest

The authors declare no conflict of interest.

## Data Availability Statement

The data that support the findings of this study are available from the corresponding author upon reasonable request.

## Keywords

conformal materials, electromagnetic metamaterials, grayscale, multifunctional materials

Received: May 24, 2022

Revised: December 8, 2022

Published online: January 31, 2023

- [1] a) X. Ni, Z. J. Wong, M. Mrejen, Y. Wang, X. Zhang, *Science* **2015**, 349, 1310; b) D. K. Nikolov, A. Bauer, F. Cheng, H. Kato, A. N. Vamivakas, J. P. Rolland, *Sci. Adv.* **2021**, 7, eabe5112; c) S. M. Kamali, A. Arbabi, E. Arbabi, Y. Horie, A. Faraon, *Nat. Commun.* **2016**, 7, 11618.
- [2] a) F. Presutti, F. Monticone, *Optica* **2020**, 7, 624; b) J. Engelberg, U. Levy, *Optica* **2021**, 8, 834.
- [3] N. Landy, D. R. Smith, *Nat. Mater.* **2013**, 12, 25.
- [4] a) D. Sell, J. Yang, S. Doshay, R. Yang, J. A. Fan, *Nano Lett.* **2017**, 17, 3752; b) W. Ma, F. Cheng, Y. Xu, Q. Wen, Y. Liu, *Adv. Mater.* **2019**, 31, 1901111; c) Z. Liu, D. Zhu, K.-T. Lee, A. S. Kim, L. Raju, W. Cai, *Adv. Mater.* **2020**, 32, 1904790.
- [5] S. Chen, W. Liu, Z. Li, H. Cheng, J. Tian, *Adv. Mater.* **2020**, 32, 1805912.
- [6] F. Callewaert, V. Velez, P. Kumar, A. V. Sahakian, K. Aydin, *Sci. Rep.* **2018**, 8, 1358.
- [7] D. Pande, J. Gollub, R. Zecca, D. L. Marks, D. R. Smith, *Phys. Rev. Appl.* **2020**, 13, 024033.
- [8] P. Camayd-Muñoz, C. Ballew, G. Roberts, A. Faraon, *Optica* **2020**, 7, 280.
- [9] a) C. Roques-Carmes, Z. Lin, R. E. Christiansen, Y. Salamin, S. E. Kooi, J. D. Joannopoulos, S. G. Johnson, M. Soljačić, *ACS Photonics* **2022**, 9, 43; b) M. Camacho, B. Edwards, N. Engheta, *Nat. Commun.* **2021**, 12, 1466.
- [10] a) D. Smith, D. Vier, T. Koschny, C. Soukoulis, *Phys. Rev. E* **2005**, 71, 036617; b) Y. Li, L. Ge, M. Chen, Z. Zhang, Z. Li, J. Wang, *IEEE Trans. Antennas Propag.* **2019**, 67, 2923.
- [11] a) J. A. Fan, D. Sell, J. Yang, The Board of Trustees of the Leland Stanford Junior University, Stanford, *US10725290B2*, **2017**; b) T. Phan, D. Sell, E. W. Wang, S. Doshay, K. Edee, J. Yang, J. A. Fan, *Light: Sci. Appl.* **2019**, 8, 48.
- [12] J. Yang, J. A. Fan, *Opt. Express* **2017**, 25, 23899.
- [13] C. Y. Kao, S. Osher, E. Yablonovitch, *Appl. Phys. B* **2005**, 81, 235.
- [14] J.-M. Jin, *The Finite Element Method in Electromagnetics*, 3rd ed., John Wiley & Sons, New York **2015**.
- [15] A. Farjadpour, D. Roundy, A. Rodriguez, M. Ibanescu, P. Bermel, J. D. Joannopoulos, S. G. Johnson, G. W. Burr, *Opt. Lett.* **2006**, 31, 2972.
- [16] a) C. Qian, B. Zheng, Y. Shen, L. Jing, E. Li, L. Shen, H. Chen, *Nat. Photonics* **2020**, 14, 383; b) R. W. Ziolkowski, *IEEE Trans. Antennas Propag.* **2003**, 51, 1516.
- [17] B. J. Justice, J. J. Mock, L. Guo, A. Degiron, D. Schurig, D. R. Smith, *Opt. Express* **2006**, 14, 8694.
- [18] S. Shrestha, A. C. Overvig, M. Lu, A. Stein, N. Yu, *Light: Sci. Appl.* **2018**, 7, 85.
- [19] W. T. Chen, A. Y. Zhu, F. Capasso, *Nat. Rev. Mater.* **2020**, 5, 604.
- [20] C. H. Schmidt, M. M. Leibfritz, T. F. Eibert, *IEEE Trans. Antennas Propag.* **2008**, 56, 737.

- [21] UIUC Airfoil Coordinates Database, [https://m-selig.ae.illinois.edu/ads/coord\\_database.html](https://m-selig.ae.illinois.edu/ads/coord_database.html) (accessed: June 2021).
- [22] W. Lijun, M. Mazilu, T. Karle, T. F. Krauss, *IEEE J. Quantum Electron.* **2002**, *38*, 915.
- [23] R. Liu, C. Ji, J. J. Mock, J. Y. Chin, T. J. Cui, D. R. Smith, *Science* **2009**, *323*, 366.
- [24] W. X. Jiang, J. Y. Chin, Z. Li, Q. Cheng, R. Liu, T. J. Cui, *Phys. Rev. E* **2008**, *77*, 066607.
- [25] H. Goh, A. Alù, *Phys. Rev. Lett.* **2022**, *128*, 073201.
- [26] M. Barbuto, Z. Hamzavi-Zarghani, M. Longhi, A. Monti, D. Ramaccia, S. Vellucci, A. Toscano, F. Bilotti, **2022**, *70*, 8883.
- [27] I. Kim, R. J. Martins, J. Jang, T. Badloe, S. Khadir, H.-Y. Jung, H. Kim, J. Kim, P. Genevet, J. Rho, *Nat. Nanotechnol.* **2021**, *16*, 508.
- [28] E. Tseng, S. Colburn, J. Whitehead, L. Huang, S.-H. Baek, A. Majumdar, F. Heide, *Nat. Commun.* **2021**, *12*, 6493.
- [29] a) M. A. Skylar-Scott, J. Mueller, C. W. Visser, J. A. Lewis, *Nature* **2019**, *575*, 330; b) J. R. Tumbleston, D. Shirvanyants, N. Ermoshkin, R. Januszewicz, A. R. Johnson, D. Kelly, K. Chen, R. Pinschmidt, J. P. Rolland, A. Ermoshkin, E. T. Samulski, J. M. DeSimone, *Science* **2015**, *347*, 1349; c) C. R. Ocier, C. A. Richards, D. A. Bacon-Brown, Q. Ding, R. Kumar, T. J. Garcia, J. van de Groep, J.-H. Song, A. J. Cyphersmith, A. Rhode, A. N. Perry, A. J. Littlefield, J. Zhu, D. Xie, H. Gao, J. F. Messinger, M. L. Brongersma, K. C. Toussaint, L. L. Goddard, P. V. Braun, *Light: Sci. Appl.* **2020**, *9*, 196.
- [30] T. Zwick, A. Chandrasekhar, C. W. Baks, U. R. Pfeiffer, S. Brebels, B. P. Gaucher, *IEEE Trans. Microw. Theory Tech.* **2006**, *54*, 1001.
- [31] O. Luukkonen, S. I. Maslovski, S. A. Tretyakov, *IEEE Antennas Wireless Propag. Lett.* **2011**, *10*, 1295.
- [32] H. Chung, O. D. Miller, *Opt. Express* **2020**, *28*, 6945.
- [33] COMSOL Multiphysics v. 5.5. [www.comsol.com](http://www.comsol.com). COMSOL AB, Stockholm, Sweden.